Light: Science & Applications (2018) 7, 17121; doi:10.1038/lsa.2017.121
Official journal of the CIOMP 2047-7538/18
www.nature.com/lsa

ARTICLE

Label-free 3D computational imaging of spermatozoon locomotion, head spin and flagellum beating over a large volume

Mustafa Ugur Daloglu[1,2,3,*], Wei Luo[1,2,3,*], Faizan Shabbir[1], Francis Lin[2], Kevin Kim[4], Inje Lee[2], Jia-Qi Jiang[5], Wen-Jun Cai[6], Vishwajith Ramesh[2], Meng-Yuan Yu[7] and Aydogan Ozcan[1,2,3,8]

We report a high-throughput and label-free computational imaging technique that simultaneously measures in three-dimensional (3D) space the locomotion and angular spin of the freely moving heads of microswimmers and the beating patterns of their flagella over a sample volume more than two orders-of-magnitude larger compared to existing optical modalities. Using this platform, we quantified the 3D locomotion of 2133 bovine sperms and determined the spin axis and the angular velocity of the sperm head, providing the perspective of an observer seated at the moving and spinning sperm head. In this constantly transforming perspective, flagellum-beating patterns are decoupled from both the 3D translation and spin of the head, which provides the opportunity to truly investigate the 3D spatio-temporal kinematics of the flagellum. In addition to providing unprecedented information on the 3D locomotion of microswimmers, this computational imaging technique could also be instrumental for micro-robotics and sensing research, enabling the high-throughput quantification of the impact of various stimuli and chemicals on the 3D swimming patterns of sperms, motile bacteria and other micro-organisms, generating new insights into taxis behaviors and the underlying biophysics.
Light: Science & Applications (2018) **7,** 17121; doi:10.1038/lsa.2017.121; published online 12 January 2018

Keywords: flagellar motion; holography; on-chip microscopy; sperm head spin; sperm tracking

INTRODUCTION

Sperm cells complete a challenging task in finding the egg, crucial for sustaining the existence of life, with a low probability of success for each cell. The swimming patterns of these remarkable microswimmers and the underlying physical processes[1] have been topics of interest for many researchers in biological fields, even before the advent of digital microscopy techniques. For example, researchers used to track individual sperm on photographic films and manually trace the trajectories of these cells, providing early insights on how individual sperm move in two-dimensional (2D) space[2–6]. With the introduction of digital cameras and improvements in digital microscopy techniques, computer-assisted sperm analysis (CASA) systems have become an important aid in both research and medical diagnostics related to microswimmers and sperms[7,8]. Such CASA systems comprise a lens-based microscope with a digital camera connected to a PC used for capturing sequential frames. These digital images are subsequently processed using custom designed software to detect and track the heads of the sperms[9]. Using conventional lens-based microscopes, existing CASA systems record the 2D trajectories of motile sperm heads, quantifying their motility by measuring curvilinear velocity (VCL), straight-line velocity (VSL), linearity, amplitude of lateral head displacement (ALH), and the beat-cross frequency (BCF), among other parameters[7,10]. In these systems, the sperm samples are observed/tracked across a rather limited depth-of-field (DOF) of ~20 μm[7,11], forcing these cells to remain in a 2D plane during imaging with a (10–20)× objective lens. This type of 2D motion analysis is widely used in medicine and animal husbandry to evaluate sperm motility[12].

In natural settings, however, sperms and many other microswimmers move within a volume, and 3D imaging and tracking of microswimmer locomotion are relatively underexplored, largely due to the inherent limitations of lens-based microscopy systems. For example, conventional lens-based microscopes have an inherent trade-off between field-of-view (FOV) and resolution, which makes it impractical to image large quantities of motile sperms in detail, particularly considering the fact that the sperm flagellum thickness is

[1]Electrical and Computer Engineering Department, University of California, Los Angeles, CA 90095, USA; [2]Bioengineering Department, University of California, Los Angeles, CA 90095, USA; [3]California NanoSystems Institute (CNSI), University of California, Los Angeles, CA 90095, USA; [4]Chemistry and Biochemistry Department, University of California, Los Angeles, CA 90095, USA; [5]Department of Physics and Astronomy, University of California, Los Angeles, CA 90095, USA; [6]Department of Mathematics, University of California, Los Angeles, CA 90095, USA; [7]Computer Science Department, University of California, Los Angeles, CA 90095, USA and [8]Department of Surgery, David Geffen School of Medicine, University of California, Los Angeles, CA 90095, USA
*These authors contributed equally to this work.
Correspondence: A Ozcan, Email: ozcan@ucla.edu
Received 27 May 2017; revised 14 August 2017; accepted 14 August 2017; accepted article preview online 16 August 2017
The accepted article preview was available with the details: *Light: Science & Applications* (2018) 7, e17121; doi: 10.1038/lsa.2017.121

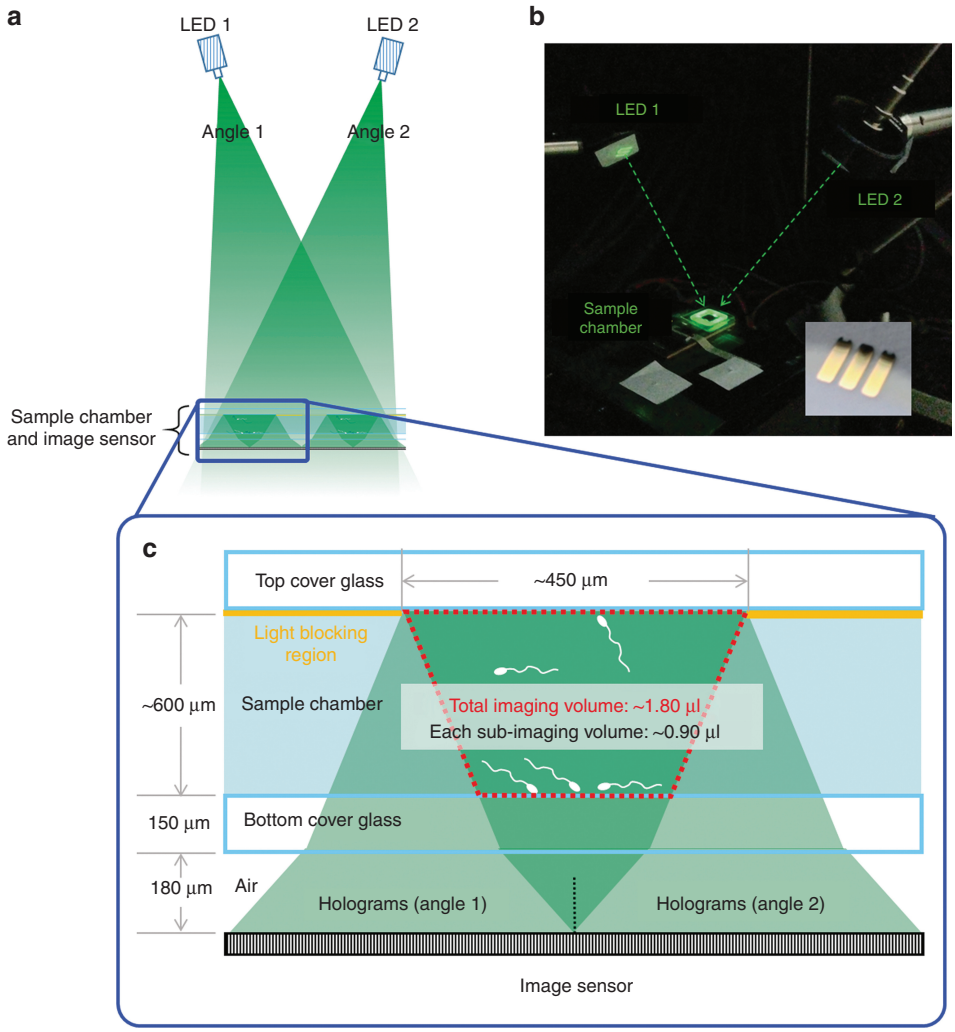

Figure 1 Optical setup. (**a**) Dual-angle 3D sperm imaging and tracking platform using a spatially structured sample holder. (**b**) A photograph of the platform with the two fiber-coupled light-emitting diodes (LEDs, ~525-nm central wavelength with ~20-nm spectral bandwidth) placed at an angle of incidence of ~18° with mirror symmetry. The sample chamber is placed directly on top of the complementary metal oxide semiconductor (CMOS) image sensor, operating at ~300 fps. The inset is a photograph of the structured substrate that is generated by depositing gold (50-nm thick) on a glass slide. (**c**) Light passing through the mask generates a pair of spatially separated holograms for each sperm cell, fully utilizing the dynamic range of the image sensor and increasing the signal-to-noise ratio (SNR) of the reconstructions. The 3D imaging volume per bright stripe (space between the gold stripes) is 0.9 µl, resulting in a total imaging volume of 1.8 µl per experiment. The DOF is ~0.6 mm and the total volume of the sperm sample placed on the sample holder is ~34 µl.

typically sub-wavelength[13–15]. Furthermore, the DOF of a lens-based microscopy system is also relatively shallow, making it hard to focus on fast moving sperm, particularly in the vertical direction (that is, cells moving away from or towards the objective lens)[16]. Another challenge reflects the fact that the sperm flagellum is long (for example, >55 µm for human sperms[13] and >65 µm for bovine sperms[14,15]) and a traditional lens-based optical microscope would not be able to image it in focus in 3D, even if high frame rates were achieved. Although there are various powerful 3D imaging modalities, such as confocal microscopy[17], light sheet microscopy[18,19] or optical coherence tomography[20–22], these techniques require optical sectioning, which relatively compromises their volumetric imaging speeds, making these techniques less practical for the 3D imaging of fast-moving objects, such as sperms.

Different imaging solutions have been proposed to circumvent some of the drawbacks of conventional lens-based microscopy systems. One approach in tracking the sperm head is to use two separate objective lenses, each imaging the same volume from two different perspectives perpendicular to each other to map the head position of the microswimmers in 3D[23]. Another approach is to place an objective lens on an oscillating stage and record the 3D volume through rapid sectioning[24,25]. However, these approaches have a small FOV of ~0.1 mm^2 and an observation volume of <2 nl, which is approximately three orders-of-magnitude smaller compared to the imaging volume of this work, and therefore have been limited to tracking only a few microswimmers at a given time period. Moreover, these previous techniques do not detect or quantify the angular spin of the head.

Holographic microscopy has become important in overcoming some of the limitations of lens-based conventional microscopy tools[26–36], particularly for microswimmer imaging and 3D tracking[10,37–47]. Taking advantage of rapid advances in image sensor technologies and computing power, lens-free on-chip imaging avoids the FOV and DOF limitations of conventional objective lenses and significantly boosts the space-bandwidth product (SBP) of the overall far-field microscopy system compared to lens-based systems[48,49] (see

doi:10.1038/lsa.2017.121

the Supplementary Information for further discussion). Using this computational microscopy framework, a holographic on-chip imaging method has recently been developed[10,44] to track the sperm head within a large sample volume ($>8\,mm^3$) with sub-micron 3D positioning accuracy. This previous approach, however, could not observe or reconstruct the 3D beating patterns of the flagellum or the spinning behavior of the sperm head due to its limited signal-to-noise ratio, contrast and frame rate. In fact, the flagellar motion of a microswimmer is much more difficult to image and reconstruct in 3D compared to head locomotion since (i) its thickness is significantly smaller (that is, sub-wavelength), and therefore the flagellum is much weaker in its scattering strength compared to the head, (ii) flagellar motion is much faster in 3D compared to the head locomotion, and (iii) its 3D beating pattern, at a given time point, spans a volume several orders of magnitude larger compared to the head, making it significantly more challenging to image; thus, the 3D imaging of the motion of sperm flagellum requires the separate localization of each sub-segment of a long 3D string as a function of time, whereas the head position at a given time point involves a single localization task, corresponding to a much stronger scattering object. These major differences necessitate a new imaging design and an entirely new set of reconstruction algorithms that enable the simultaneous 3D dynamic imaging of the sperm head and flagellum as well as the spinning behavior of the head, all at the same time and over large sample volumes.

Here we report a high-throughput and label-free computational holographic microscope (Figure 1) that can simultaneously reconstruct the complete 3D locomotion details of freely moving microswimmers, including the translation and spin of the head and the beating pattern of the flagellum, all at the same time and over a large observation volume of $\sim 1.8\,\mu l$, spanning a large depth-of-field of $\sim 0.6\,mm$. In this imaging configuration, the specimen containing live sperms is placed on top of an opto-electronic image sensor chip without using any imaging optics or lenses and simultaneously illuminated by two sources (each partially coherent) emerging from two oblique angles. Large volume 3D tracking of microswimmers and real-time 3D position estimation of micro-objects have been enabled by this lens-free imaging technique[10,44,45,50]. Dual-angle illumination in holography has also been used for the 3D tracking of particles using lens-based platforms[51,52]; however, with limited throughput due to the trade-off between FOV (or sample volume) and spatial resolution. In the present study, we also significantly improved this dual-angle lens-free imaging platform using a structured substrate (Figure 1), designed with a periodic light-blocking mask placed on top of the sample holder. This mask spatially separates the two holographic projections of the sperms generated according to the oblique illumination angles, which enables the full utilization of the dynamic range of the image sensor chip, an important advance necessary to simultaneously detect the holograms of the optically weaker flagella from two different perspectives. In addition, to record the rapid motion of the flagella in 3D, the frame readout rate of this platform was increased to 300 ± 3 fps using a custom-designed image readout circuitry, which is critical to record the flagellar motion without undersampling. We also developed a unique 3D image reconstruction framework that first calculates the 2D holographical projections of the moving sperms along both of the illumination directions, and subsequently uses this information to compute the 3D beating patterns of the sperms' flagella and track the motion of the sperm heads. Moreover, using successive phase wrapping events occurring in each 2D projection, when the illumination light traverses through the sperm head along its thicker side, the same holographic image reconstruction framework enabled the determination of the spin direction of the sperm head and its angular velocity.

Using this label-free computational imaging platform running at ~ 300 fps we recorded over 2100 individual trajectories of freely swimming bovine sperms, and measured, all in parallel and in 3D, their head motion and spin, and the flagellar beating patterns. In addition to high-throughput quantification of various dynamic swimming parameters[10], including, for example, VCL, VSL, linearity, ALH, BCF and head spin, we also categorized these measured swimming patterns[10,44,45] according to their translational mode: namely, helix (45%), random (32.2%), helical ribbon (12.1%), twisted ribbon (2.4%), flat ribbon (2.1%), slithering (3.8%) and straight spin (2.4%). Detection of the sperm head spin revealed that 100% of the spinning sperms (2053 in total) in free space exhibited a right-handed spin along the head spin axis from the perspective of the rear of the sperm. We also performed harmonic analysis on the measured 3D flagella beating patterns, conducted in a local coordinate system that also moves and spins together with the sperm head, and therefore decouples the flagellum beating patterns from sperm head translation and spin, which otherwise would generate significant errors in any related analysis. Resulting from this local coordinate system, we found that in the two basic swimming modes, that is, helix and slithering, whether the sperm head is spinning or not, the flagellum exhibits approximately planar and sinusoidal waves that propagate from the mid-piece of the flagellum toward its end with growing amplitudes (that is, a sinusoidal wave within the envelope of a growing exponential).

We propose that this high-throughput and label-free computational microswimmer imaging platform not only provides unmatched capabilities for the measurement of 3D locomotion patterns of microswimmers, but also lays the foundation for new imaging tools and insights that can be transformative in micro-robotics and sensing-related research and applications. Furthermore, this imaging technique might provide a high-throughput tool to rapidly quantify the impact of various stimuli on the 3D swimming patterns of sperms and other motile micro-organisms, leading to new insights into 3D locomotion and taxis behaviors.

MATERIALS AND METHODS

Label-free and 3D reconstruction of the locomotion of freely moving sperm: head and flagellum

This holographic on-chip imaging platform features dual-angle illumination (Figure 1), and a numerical reconstruction framework to retrieve the complete set of details of 3D swimming patterns of microswimmers at ~ 300 fps, including the head translation, flagellum beating and the sperm head spin. In this on-chip imaging platform, the light scattered by the entire body of the sperm and the directly transmitted light from each LED form interference patterns (that is, in-line holograms) of the moving cells on top of the image sensor chip, which are subsequently digitized for reconstruction. No focusing lens or image projection system is needed during the data acquisition since we can numerically focus on different sections of the object volume using digital wave propagation. The use of dual-angle illumination in on-chip imaging significantly improves the depth localization accuracy since triangulating the reconstructions from two perspectives, enabling the calculation of the height and lateral position of the specimen. This 3D tracking process, however, is much simpler for tracking the sperm head compared to the flagellum since the latter (1) is much larger in length compared to the head and therefore requires a significantly larger tracking volume per sperm to reveal the 3D functional form of the flagellum; (2) is much weaker in hologram

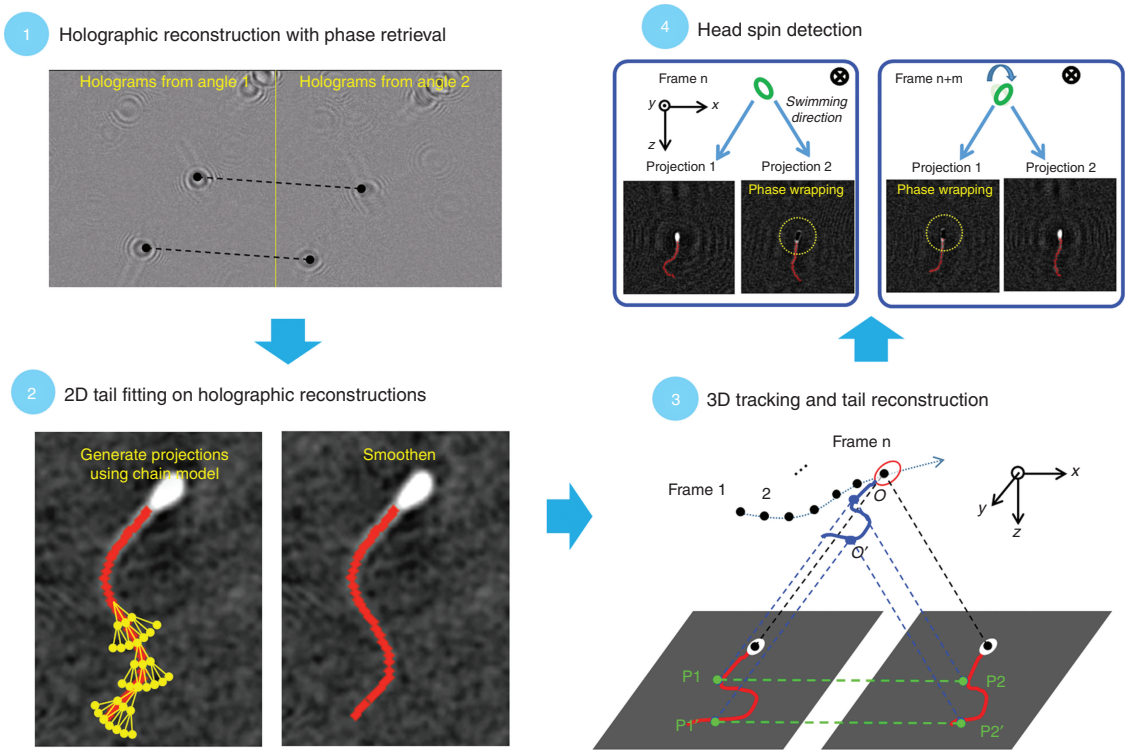

Figure 2 3D reconstruction of sperm locomotion. Step 1: Background-subtracted holograms resulting from dual-angle illumination undergo a holographic reconstruction process, which uses object support-based phase retrieval to mitigate the twin image artifact. Step 2: A two-dimensional tail fitting process is performed on these holographic reconstructions to establish the skeletons corresponding to both of the 2D projections of the sperm flagellum. These fitted skeletons are subsequently spatially smoothened and interpolated into 2D strands with a smaller node length. Step 3: 3D tracking and tail reconstruction. Based on the two illumination angles and corresponding projections, the height of each infinitesimal sub-section along the 3D strand is determined, and the 3D configuration of the entire strand, representing the flagellum, is reconstructed. This reconstruction process is also detailed in the Supplementary Information section and Figure 3. Step 4: Alternating phase-wrapping events between the two holographic reconstructions are used to determine the head spin direction and angular velocity (also detailed in the Results and Discussion section).

intensity since the flagellum is a sub-wavelength in its thickness whereas the sperm head is much thicker; and (3) moves much faster in 3D space making it significantly harder to track compared to the sperm head. In fact, due to these challenges, existing techniques, lens-free or lens-based, have not yet been able to retrieve the complete details of 3D motion of freely swimming sperms, and could not resolve the simultaneous 3D head translation, spin and flagellum beating of these cells.

The 3D morphology of the sperm can be simplified as a tri-axial scalene ellipsoid, representing the sperm head, with a single strand attached to one end of its semi-major axis, representing the flagellum. Based on this assumption, 3D microswimmer imaging can be treated as a localization task, where the reconstruction accuracy could be much higher than the pixel pitch of the image sensor chip[10]. In principle, 2D projections at high-frame rates from only two perspectives could be used to obtain a 3D reconstruction of the sperm flagellum only if the image depth-of-field, contrast and SNR for each perspective are sufficiently large. As shown in Figures 1 and 2, the holographic on-chip imaging platform can perform this challenging task over a large observation volume of ~1.8 μl and reconstruct the complete motion of the entire sperm body in 3D using two holographic projections generated through dual-angle illumination. One key element in this 3D reconstruction process is a periodically structured substrate (Figure 1) used to spatially separate the two holographic perspectives from each other, thereby increasing the dynamic range, contrast and SNR of each reconstructed perspective of freely moving sperms. The other two important features critical for the success of this platform are high frame rate[7] (~300 fps) and a unique 3D reconstruction algorithm developed to resolve the simultaneous 3D flagellar beating and head locomotion and spin of these cells.

The reconstruction process (Figure 2) starts with the numerical back-propagation[53] of each hologram to the object plane, where the 2D projections of the sperm body (head and flagellum) can be initially obtained. However, at a given object plane digitally focused on various parts of the sperm, the flagellum can be out of focus due to the 3D nature of the flagellum, which is mitigated by additional processing, as detailed later in this study. To enhance the visibility of the holograms generated by motile sperms, we subtracted the moving average of ~ 100–200 frames (empirically selected) from each of the original holograms, so that the holographic signatures of immotile sperm and other stationary or unwanted objects are markedly suppressed (Figure 2, step 1). This numerical back-propagation also features an iterative, object-support-based phase retrieval technique[54], which mitigates the twin image noise and thus improves the digital extraction of each flagellum projection (Figure 2, step 2).

The projection of the sperm flagellum from each angle is a 2D strand parallel to the image sensor plane, which can be obtained after fitting a skeleton to the reconstructed phase map. The 2D skeleton itself is digitally generated through a chain of equally spaced points set at 3 μm apart. The automated skeleton fitting process for each perspective initiates from the head-flagellum junction, and 5 new

doi:10.1038/lsa.2017.121

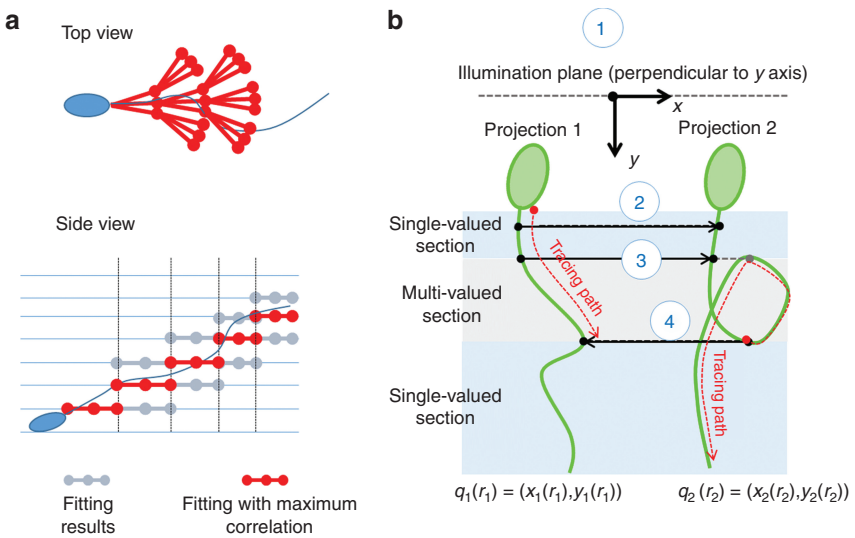

Figure 3 (**a**) Generation of the 2D skeleton for each projection. Each 2D skeleton is generated through a multi-step fitting process initiated from the head–flagellum junction (top view). To avoid early termination of tail fitting due to out-of-focus reconstruction at one height, each hologram is also reconstructed at its neighboring heights (for example, ±15 μm from the original reconstruction height). **(b)** A 4-step, point-tracking algorithm, which resolves the ambiguities of projection paring, reconstructs the 3D configuration of the flagellum (Supplementary Information for details).

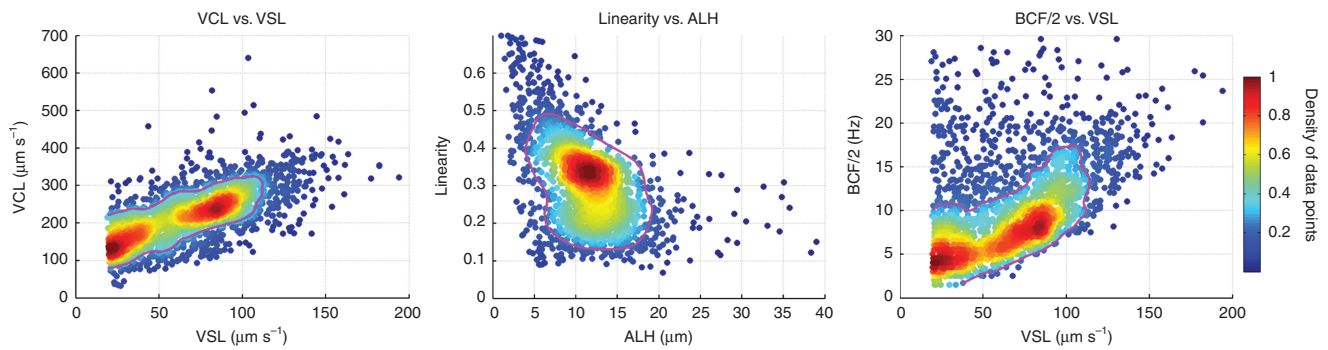

Figure 4 The dynamic swimming parameters from 2133 bovine sperm trajectories. The magenta curve encloses 70% of all data points, and the color bar on the right represents the relative density of data points. ALH, amplitude of lateral head displacement; BCF, beat-cross frequency; VCL, curvilinear velocity; VSL, straight-line velocity. Please refer to the Supplementary Information for detailed definitions of these parameters.

connected points are added at each step of this iterative process, where the first point connects to the end of the previously fitted section of the chain. We typically employ $M = 4$ steps to define a skeleton for each one of the two projections. For each step, multiple uniformly spaced angles, covering an angular range of ±40°, are tested within the object plane for the assignment of each new point to the chain (Figure 2). At each step of this search process for the skeleton, each potential sub-section, comprising 5 points, is scored as the sum of the phase values at these 5 points along the skeleton. The chain with the highest score among all options is used as the new sub-section of the 2D flagellum projection, and this skeleton growth iterates until the score for all potential solutions falls below the noise level (that is, the background phase variance) of the phase reconstructions. The positions of the points in each 2D flagellum skeleton are further optimized using PSF (point spread function) fitting along the phase profile[55], and finally a spline fitting (interpolation) is performed to obtain a smoothened 2D strand with a node length of ~0.19 μm.

Reflecting the 3D nature of the flagellum, the holographic reconstruction at a single height is insufficient because some sections of the flagellum may be far away from the reconstruction height and become out-of-focus, resulting in the early termination of the above-described skeleton-fitting process. To avoid this effect, we also implemented an extended search strategy (depicted in Figure 3a): when the score of all the potential sub-skeletons on a given reconstruction height/plane falls below the noise threshold, the hologram is reconstructed at its neighboring heights (for example, ±15 μm from the original reconstruction height) and the sub-skeleton-fitting process is continued at each new height. The plane with the highest fitting score is selected as the final reconstruction height at that sub-section of the flagellum. This fitting process per sperm terminates when the sub-skeleton-fitting scores at all heights fall below the noise level.

The 3D reconstruction of the flagellum from these 2D skeletons calculated in the previous step is also a progressive process (Figure 2, step 3 and Figure 3), where a pair of points from the two 2D skeletons is used to triangulate the corresponding 3D points on the flagellum at each step of this 3D reconstruction process (refer to the Supplementary Information section for more details). This 3D pairing is automatically performed, identifying the two points that fall in the same illumination plane defined by the two illumination directions. Traversing through the two 2D skeletons of each perspective while

triangulating these intersection points, the 3D functional form of the flagellum at a given time point is obtained (sampled at 300 fps). Notably, ambiguity could arise during this 3D reconstruction process when there are multiple points that reside within the same illumination plane on a 2D strand (Figure 3b). Such ambiguity can be resolved by considering that the pairing should progress in continuous increments along the arc length on both of the projections without sudden jumps. Therefore, when multiple candidate points for pairing are encountered on one of the projections, the unpaired point with the shortest arc length is selected as the correct point to match.

The uniqueness of this 3D flagellum reconstruction is guaranteed when no subsections of each 2D skeleton is parallel to the illumination plane. The non-uniqueness of this 3D reconstruction is only observed, momentarily, when the flagellum is precisely parallel to the illumination plane, corresponding to a very small fraction of the cells within the large specimen volume that is imaged (~1.8 μl). More importantly, the unique flagellar motion of the sperm can be recovered rapidly as soon as the flagellum starts to have components that are orthogonal to the illumination plane. The small portion of the sperms that violate the 3D flagellum reconstruction uniqueness does not compromise the high throughput of our sperm imaging and tracking platform. Refer to the Supplementary Information section and Figure 3b for a detailed discussion of the uniqueness of these 3D flagella reconstructions.

RESULTS AND DISCUSSION

Using the presented label-free computational imaging framework, we reconstructed the 3D locomotion of 2133 bovine sperms (Figure 4 for some of the dynamic swimming parameters measured from these reconstructed trajectories), consistent with previously reported values for bovine sperm locomotion measured using conventional CASA systems[56]. Examples of 3D head tracks, spins and flagellar beating patterns are also illustrated in Figures 5 and 6; Supplementary Figs. S3 to S9, and Supplementary Movies M1 through M6. Although previous studies using conventional lens-based microscopes showed some flagellar beating patterns for 2D restricted sperms[57,58], the results of the present study provide the first complete reconstruction of the 3D motion of freely moving sperms, including their head translation (Figure 4), rotation/spin (Figures 5, 6 and 7), and flagellar beating patterns (Figures 5 and 6). Moreover, this imaging platform does not use any fluorescent labeling or confine the sperms to smaller volumes or surfaces, and therefore it truly captures the natural locomotion of the sperms in 3D without any external perturbations to the cells. As another major advantage, the sample volume probed in this on-chip imaging technique is ~1.8 μl, which is approximately three orders of magnitude larger compared to previous approaches[24], generating a significant sample throughput that can be used to reveal various statistically rare features of the 3D locomotion of sperm, as detailed in the next sections.

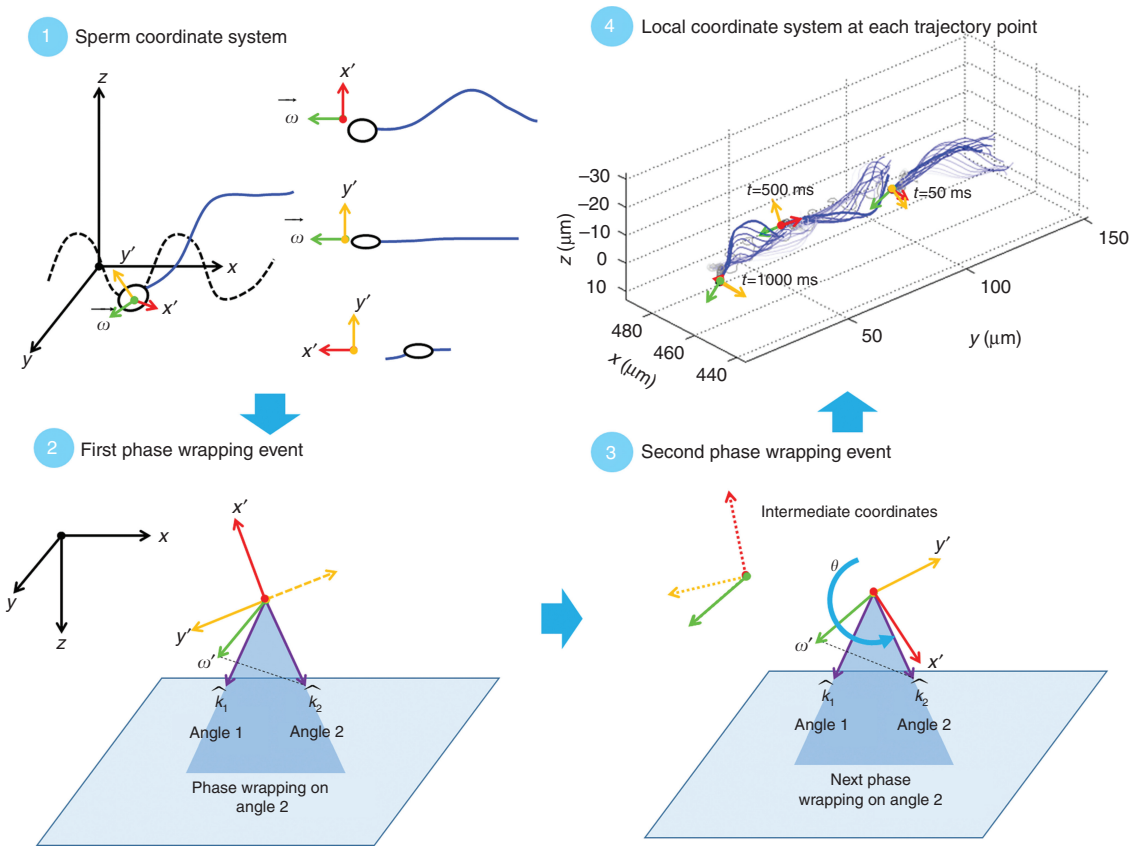

Figure 5 Establishing a local coordinate system for the representation of head spin. Step 1: Define a local Cartesian coordinate system where the $\vec{\omega}$ is the spin axis, that is, the semi-major axis of the ellipsoidal, and the local x', y' axes are the longer and shorter semi-minor axes, respectively. Step 2: At the first phase wrapping event (for example, on projection 2), given that the illumination vector is within x'-$\vec{\omega}$ plane and the spin axis $\vec{\omega}$ can be determined through 3D tail reconstruction, define the local coordinate system (x', y' and $\vec{\omega}$). Step 3: Determine the value of the spin angle between the first and second phase wrapping events by comparing the rotation of the local coordinates' around $\vec{\omega}$ axis. Step 4: Determine the spin angle for all the frames, at 300 fps (also Supplementary Fig. S1).

doi:10.1038/lsa.2017.121

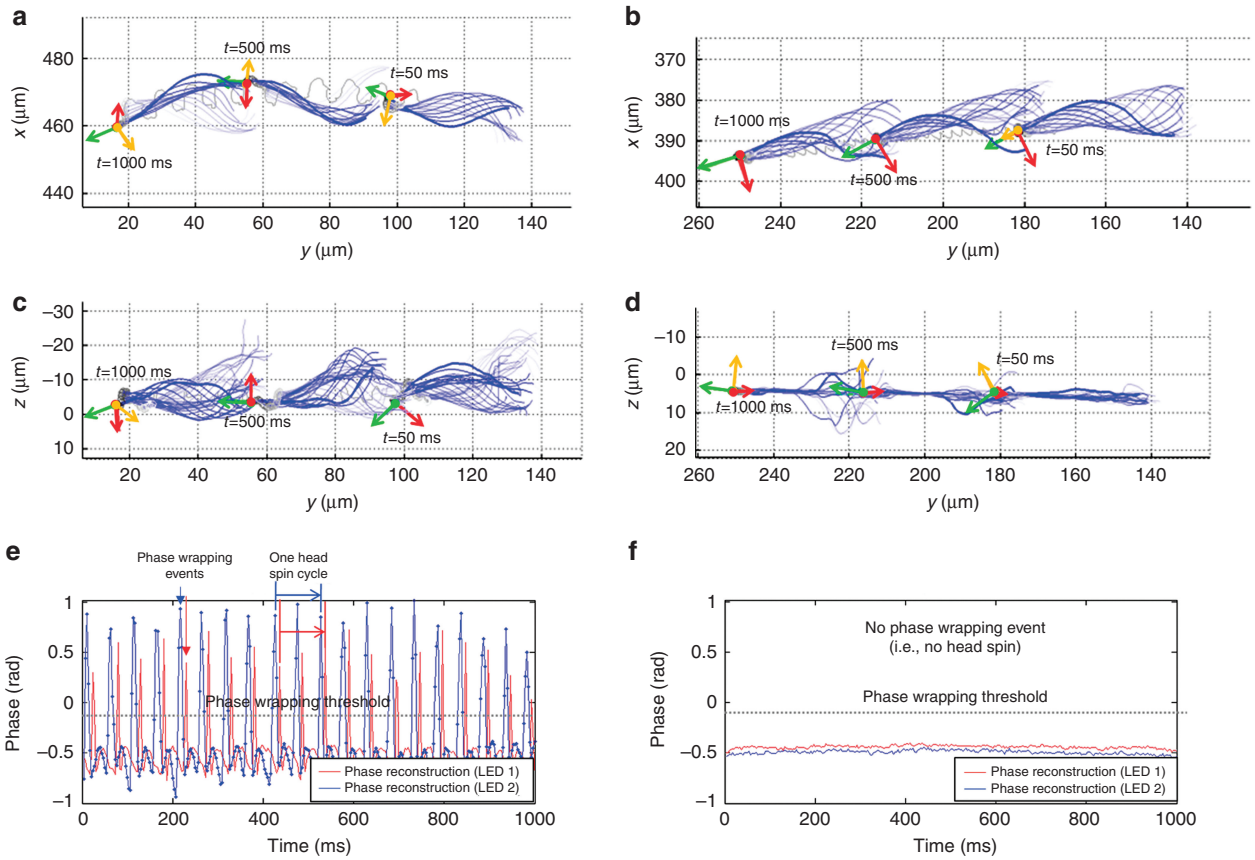

Figure 6 Two major swimming modes of sperm motion: helix mode and slithering (that is, non-rotational) mode. (**a**) and (**b**) Top view (***x***–***y*** plane in global coordinates) of the helix mode and the slithering mode, respectively. (**c**) and (**d**) Side view (***z***–***y*** plane in global coordinates) of the helix mode and the slithering mode, respectively. (**e**) and (**f**) The phase value of the sperm head projections as a function of time. The order of the phase wrapping events from the two projections indicates the spin direction of the sperm head. The 3D motion of the sperm head and flagellum in **a**, **c** and **e** are shown in Supplementary Movie M1, and the 3D motion of **b**, **d** and **f** are shown in Supplementary Movie M2.

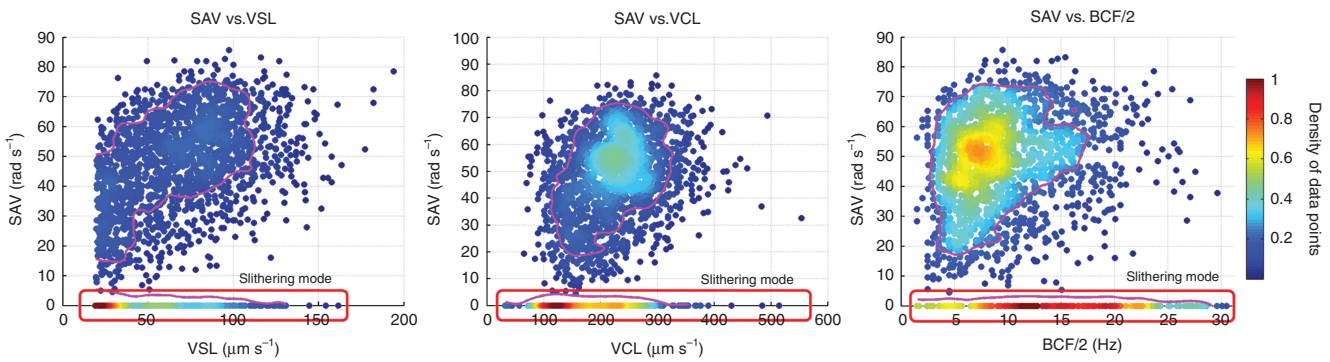

Figure 7 The angular velocity (in rad s^{-1}) of sperm head spin compared to the dynamic swimming parameters corresponding to >2100 bovine sperm trajectories. The data points enclosed in red represent the parameters from slithering sperm trajectories, which do not exhibit head spin, and therefore have zero angular head spin velocity. The magenta curve encloses 70% of all the data points, where the point density is higher than the magenta boundary. The color bar on the right represents the relative density of data points. BCF, beat-cross frequency; VCL, curvilinear velocity; VSL, straight-line velocity.

High-throughput detection and analysis of sperm head spin

An interesting property of the sperm is that when the light travels through the 'thicker side' of the sperm head (parallel to the plane defined by the two minor axes), the increase in the optical path length is larger than half a wavelength. Thus, when the thicker side of the sperm head is parallel to one of the illuminations, phase wrapping occurs in the corresponding 2D holographic reconstruction (Step 4 in Figure 2 and Figure 6e). Since the orientation of the major axis can be automatically determined by connecting the sperm head center and the head–flagellum junction, at each phase wrapping event, we can determine the 3D orientation of the sperm head. These successive phase wrapping events that alternate in time between sperm head reconstructions from each perspective of the dual illumination scheme reveal, over a large volume, both the spin direction and spin angular

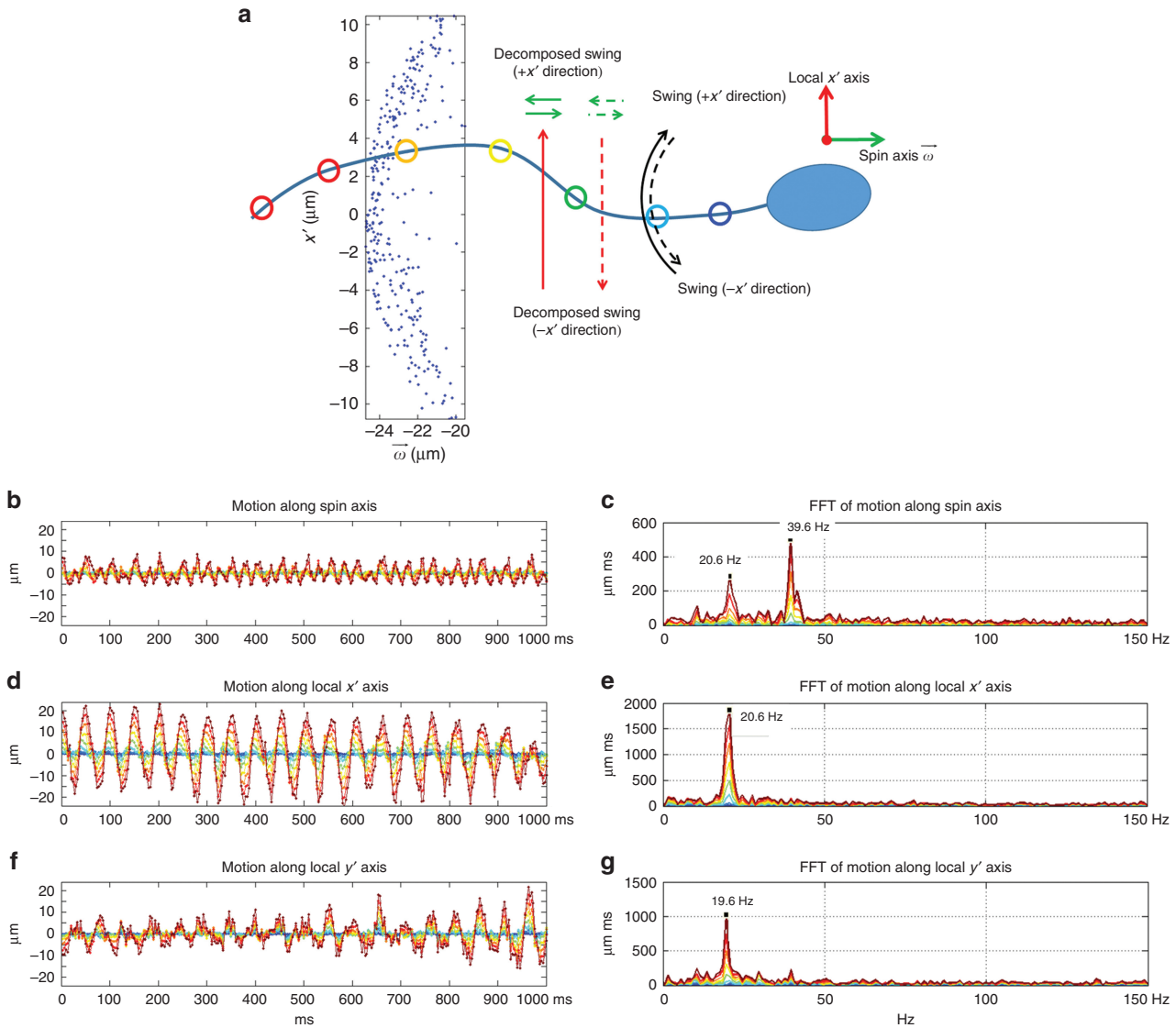

Figure 8 Waveform analysis of the flagellar beating of a helix mode bovine sperm in the local coordinate system, in both the time and frequency domains. (**a**) The analysis is performed over time, on nodes spaced with 5 μm intervals across the flagellum. Note that for one beating cycle, each node moves back and forth once in the local x' axis but twice in the spin axis $\vec{\omega}$. The inset shows the positions of a node (40 μm away from the head-flagellum junction in arc length) on the local x'–$\vec{\omega}$ plane over time. (**b**), (**d**) and (**f**) The node positions along the spin axis $\vec{\omega}$, the local x' and the local y' axis, respectively, are plotted against time. These waveforms are color-coded based on the colors of the corresponding nodes in **a**. (**c**), (**e**) and (**g**) The same waveforms are represented in the frequency domain according to their Fourier transformations with respect to time. The 3D motions of the sperm head and flagellum for the helix mode are shown in Supplementary Movie M1.

velocity of the sperm head (Figure 6 and Supplementary Fig. S1), which could not be simultaneously measured in freely moving sperm samples prior to this work.

To make better use of this angular spin measurement and represent the orientation of the sperm head accurately, we also defined a local Cartesian coordinate system with axes x', y' and $\vec{\omega}$ (depicted in Figure 5), where the $\vec{\omega}$ is the spin axis, that is, lies in the direction of the semi-major axis of the ellipsoidal, and the local x', y' axes are the longer and shorter semi-minor axes, respectively (Supplementary Information and Figures 5 and 6 for details). As discussed in the following sub-section, this local coordinate system is important to accurately analyze the 3D flagellar beating patterns. Using this local coordinate system, we measured the spin angular velocities (SAV) of 2133 bovine sperms and the VCL, VSL, ALH and BCF[10]. Based on these measurements, Figure 7 shows the density map of SAV vs. VCL, VSL and BCF, where the mean value of the sperm head SAV is ~48 rad s^{-1} (that is, 7.6 revolutions per second), with a standard deviation of ~16 rad s^{-1}. For sperms exhibiting head spin during locomotion, SAV is generally higher when the VCL, VSL and BCF are larger, that is, the sperms that swim faster also spin faster. Notably, this observation could not be reported using existing techniques, which either immobilize the sperms onto a surface or severely restrict their locomotion in space, also limiting the throughput of such measurements. These results also reveal that all the spinning sperms show right-handed head spin, consistent with previous reports on hamster sperms[59], which are much easier to observe since the spin of their hook-shaped heads can be directly observed in 2D using a conventional lens-based microscope due to the unique shape and large size of

doi:10.1038/lsa.2017.121

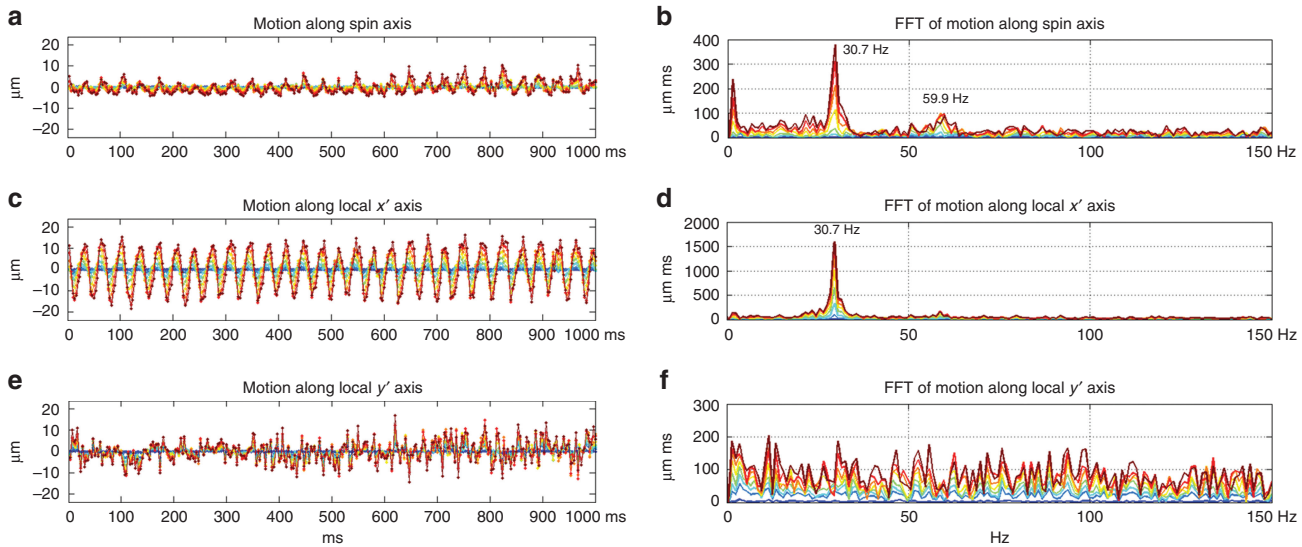

Figure 9 Same as Figure 8, except depicting the slithering rather than the helix mode, bovine sperms represented in the local coordinate system. Unlike the helix mode shown in Figure 8, the slithering mode sperm is close to the chamber surface and the sperm head does not spin during the motion. It is apparent from both the time and frequency domain plots that the flagellar beating is confined within the $\boldsymbol{x}'$–$\vec{\omega}$ plane, and there is no apparent peak in the local $\boldsymbol{y}'$ for the slithering mode sperm. Similar to the helix mode, a double frequency is also observed along the spin axis $\vec{\omega}$ in addition to an increase in waveform amplitude along the sperm flagellum. The 3D motion of the sperm head and flagellum for the slithering mode is shown in Supplementary Movie M2.

these sperm. In general, the angular spin of the sperm head provides evidence for coordinated sliding in the microtubules of the axoneme[60–62].

As shown in Figure 7, a considerable portion of the sperms (3.8%) does not exhibit angular spin, although they have fast translational trajectories. These non-spinning sperms, namely 'slithering sperms', are located at either the bottom or the top surface of the sample chamber. Their entire motion, including the flagella, is confined in the vertical direction within ~ 10 µm from the surface, as shown in Figure 6b and 6d, with the corresponding flagellar beating patterns. These results also highlight the importance of the 3D imaging of freely moving sperm over large sample volumes and depths-of-field, as in the technique presented herein, since the presence of a surface, although convenient for lens-based microscopic imaging, fundamentally alters the 3D locomotion of sperms.

Frequency analysis of the flagellar beating patterns

From the perspective of the global coordinate system of the image sensor chip in the present imaging technique or any microscopic imaging modality in general, the motion of the flagellum reflects the combination of the 3D translation, head spin and flagellum beating of the sperm; therefore, several different types of motion affect and directly determine the mathematical representation of the flagellar beating patterns when using such a global coordinate system. However, to better understand the flagellar kinematics of the sperm, it is desirable to isolate the 3D beating pattern that is only related to the flagellum itself, taking out the effects of head locomotion and spin. Obtaining the complete 3D information of freely moving sperm enables the decoupling of the flagellar beating patterns of the sperms from their head locomotion and spin, thereby enabling the observation of flagella beating under a local coordinate system that moves and spins together with the sperm head. Stated differently, we can obtain the perspective of an observer located on and moving with the sperm head, looking towards the flagellum, which isolates the sperm flagellar beating from other sources of motion (Figure 5).

To examine the beating patterns in this local coordinate system, we selected a sequence of nodes along the flagellum and tracked their positions over time (Figure 8a). The motion of each node can be decomposed along the three axes of the local coordinates and analyzed as flagellar beating waveforms over time (Figures 8 and 9). To demonstrate the significance of decoupling the head spin and locomotion prior to analyzing the flagellar dynamics, we selected two major swimming patterns (helix and slithering modes, Supplementary Table 1)[63] and studied their flagellar beating patterns using both the local and global coordinate systems (Supplementary Fig. S2). For the helix mode, the sperm head is spinning throughout the entire sperm motion (Figure 6a, 6c and 6e). From the perspective of the image sensor or the global coordinate system, this head spin also couples into the flagellar beating pattern and therefore the motion of a node on the flagellum exhibits circular patterns over time, reflecting the head spin (Supplementary Fig. S2a and S2c). However, when the head spin is decoupled from flagellar motion under a local coordinate system, the amplitude difference between the waveforms in the local $\boldsymbol{x}'$ and $\boldsymbol{y}'$ directions (Figure 8d and 8f) suggests broken circular symmetry and a 'swinging' pattern predominantly confined to the local $\boldsymbol{x}'$-$\vec{\omega}$ plane (Supplementary Fig. S2b and S2d and Supplementary Movie M6). The beating frequency of the flagellum can be determined by finding the peaks in the Fourier transform of these waveforms. For example, the beating frequency in $\boldsymbol{x}'$ and $\boldsymbol{y}'$ directions (Figure 8e and 8g) suggests that the flagellum beating pattern can be approximated as a 20-Hz sinusoidal wave. Moreover, the waveforms of different nodes in Figure 8d clearly show that as the corresponding arc length of the node from the head–flagellum junction increases, the amplitude of the waveform also increases, and there is a phase delay of the waves that have larger amplitudes. These observations suggest that the flagellum beating pattern is approximately a planar, travelling sinusoidal waveform parallel to the local $\boldsymbol{x}'$–$\vec{\omega}$ plane, and it originates from the midpiece of the flagellum with growing amplitude towards its end. Interestingly, the same harmonic analysis in the spin axis $\vec{\omega}$ also shows a second peak at double the original frequency, that is, ~ 40 Hz, which can be interpreted as additional evidence of a planar beating

pattern. As illustrated in Figure 8a, the planar swing of the flagellum will cause this double frequency along the $\vec{\omega}$ axis since the projection of each node travels back and forth twice along $\vec{\omega}$ direction during one swing period, while the projections on $\boldsymbol{x}'$ and $\boldsymbol{y}'$ directions travel only once per cycle.

For the slithering mode (3D configuration shown in Figure 6b and 6d) the sperm is close to the bottom surface of the observation chamber and the head does not spin, unlike the helix mode. In this mode of locomotion, as shown in Figure 9, the sperm flagellar beating is more strictly confined within the $\boldsymbol{x}'$-$\vec{\omega}$ plane, and there is no dominant frequency in the local $\boldsymbol{y}'$ direction. Similar to the helix mode, the flagellar beating pattern forms a travelling sinusoidal wave with growing amplitude as it propagates from the mid-piece toward the end of the flagellum. The comparison of these two modes of locomotion in this local coordinate system suggests that the major difference in their swimming patterns reflects the presence of the sperm head spin, while the flagellar locomotion mechanism remains similar. The analysis of the remaining swimming patterns is provided in the Supplementary Information section.

CONCLUSIONS

We developed a high-throughput, label-free holographic imaging platform to reconstruct the full 3D details of freely swimming sperm cells across a large sample volume two orders of magnitude larger than conventional lens-based systems used for tracking of sperms. Running at ~300 frames per second, this imaging platform features lens-free on-chip holography with dual-angle illumination, and a spatially structured mask to maximize the dynamic range and signal-to-noise ratio. The hologram pairs originated from the scattering of sperm head and flagellum are used to not only obtain the 3D translational motion of the sperm head but also the spin of the sperm head and 3D flagellar beating patterns. This platform also enables an examination of the sperm from a new perspective: by adopting a 'local' coordinate system that translates and rotates together with the sperm head, the motion of a beating flagellum can be decoupled from head translation and spin, and the 3D spatio-temporal kinematics of the flagellum can be analyzed. The large imaging volume of the platform revealed the full 3D dynamics of 2133 bovine sperm cells. By providing unprecedentedly rich information on the 3D locomotion of microswimmers, this platform might be particularly beneficial for biological and biophysical studies, involving sperm viability, quality or even its DNA content for sex sorting. In addition, this computational imaging method could also be transformative for micro-robotics and sensing-related applications.

CONFLICT OF INTEREST

The authors declare no conflict of interest.

AUTHOR CONTRIBUTIONS

MD and WL conducted the experiments and processed the resulting data. FS, FL, KK and IL contributed to the experiments and subsequent data analyses. JJ, WC, VR and MY contributed to the data analyses. MD, WL and AO planned and executed the research, and wrote the manuscript. AO supervised the project.

ACKNOWLEDGEMENTS

The Ozcan Research Group at UCLA gratefully acknowledges the support of the Presidential Early Career Award for Scientists and Engineers (PECASE), the Army Research Office (ARO; W911NF-13-1-0419 and W911NF-13-1-0197), the ARO Life Sciences Division, the National Science Foundation (NSF) CBET Division Biophotonics Program, the NSF Emerging Frontiers in Research and Innovation (EFRI) Award, the NSF EAGER Award, NSF INSPIRE Award, NSF Partnerships for Innovation: Building Innovation Capacity (PFI:BIC) Program, Office of Naval Research (ONR), the National Institutes of Health (NIH), the Howard Hughes Medical Institute (HHMI), Vodafone Americas Foundation, the Mary Kay Foundation, Steven & Alexandra Cohen Foundation, and KAUST. This work is based upon research performed in a laboratory renovated by the National Science Foundation under Grant No. 0963183, which is an award funded under the American Recovery and Reinvestment Act of 2009 (ARRA).

1 Battle C, Broedersz CP, Fakhri N, Geyer VF, Howard J *et al.* Broken detailed balance at mesoscopic scales in active biological systems. *Science* 2016; **352**: 604–607.
2 Acott TS, Katz DF, Hoskins DD. Movement characteristics of bovine epididymal spermatozoa: effects of forward motility protein and epididymal maturation. *Biol Reprod* 1983; **29**: 389–399.
3 Keller JB, Rubinow SI. Swimming of flagellated microorganisms. *Biophys J* 1976; **16**: 151–170.
4 Gray J. The movement of the spermatozoa of the bull. *J Exp Biol* 1958; **35**: 96–108.
5 Rikmenspoel R. The tail movement of bull spermatozoa: observations and model calculations. *Biophys J* 1965; **5**: 365–392.
6 Ishijima S, Hamaguchi MS, Naruse M, Ishijima SA, Hamaguchi Y. Rotational movement of a spermatozoon around its long axis. *J Exp Biol* 1992; **163**: 15–31.
7 Mortimer ST. CASA—practical aspects. *J Androl* 2000; **21**: 515–524.
8 Mortimer ST, van der Horst G, Mortimer D. The future of computer-aided sperm analysis. *Asian J Androl* 2015; **17**: 545–553.
9 Amann RP, Waberski D. Computer-assisted sperm analysis (CASA): Capabilities and potential developments. *Theriogenology* 2014; **81**: 5–17.
10 Su TW, Xue L, Ozcan A. High-throughput lensfree 3D tracking of human sperms reveals rare statistics of helical trajectories. *Proc Natl Acad Sci USA* 2012; **109**: 16018–16022.
11 DRM-600 CELL-VU® sperm counting chamber. Available at http://cellvu.com/products/drm-600-cell-vu-sperm-counting-chamber/ (accessed on September 2016).
12 Liu J, Leung C, Lu Z, Sun Y. Human sperm tracking, analysis, and manipulation. In: Rakotondrabe Meditors. *Smart Materials-Based Actuators at the Micro/Nano-Scale*. Springer: New York, NY, USA. 2013, pp251–264.
13 Smith DJ, Gaffney EA, Blake JR, Kirkman-Brown JC. Human sperm accumulation near surfaces: a simulation study. *J Fluid Mech* 2009; **621**: 289–320.
14 Bahr GF, Zeitler E. Study of bull spermatozoa. Quantitative electron microscopy. *J Cell Biol* 1964; **21**: 175–189.
15 Pesch S, Bergmann M. Structure of mammalian spermatozoa in respect to viability, fertility and cryopreservation. *Micron* 2006; **37**: 597–612.
16 Krzyzosiak J, Molan P, Vishwanath R. Measurements of bovine sperm velocities under true anaerobic and aerobic conditions. *Anim Reprod Sci* 1999; **55**: 163–173.
17 Minsky M. Memoir on inventing the confocal scanning microscope. *Scanning* 1988; **10**: 128–138.
18 Huisken J, Swoger J, Del Bene F, Wittbrodt J, Stelzer EHK. Optical sectioning deep inside live embryos by selective plane illumination microscopy. *Science* 2004; **305**: 1007–1009.
19 Planchon TA, Gao L, Milkie DE, Davidson MW, Galbraith JA *et al.* Rapid three-dimensional isotropic imaging of living cells using Bessel beam plane illumination. *Nat Methods* 2011; **8**: 417–423.
20 Huang D, Swanson EA, Lin CP, Schuman JS, Stinson WG *et al.* Optical coherence tomography. *Science* 1991; **254**: 1178–1181.
21 Tearney GJ, Brezinski ME, Bouma BE, Boppart SA, Pitris C *et al.* In vivo endoscopic optical biopsy with optical coherence tomography. *Science* 1997; **276**: 2037–2039.
22 de Boer JF, Cense B, Park BH, Pierce MC, Tearney GJ *et al.* Improved signal-to-noise ratio in spectral-domain compared with time-domain optical coherence tomography. *Opt Lett* 2003; **28**: 2067–2069.
23 Drescher K, Leptos KC, Goldstein RE. How to track protists in three dimensions. *Rev Sci Instrum* 2009; **80**: 014301.
24 Silva-Villalobos F, Pimentel JA, Darszon A, Corkidi G (eds). Imaging of the 3D dynamics of flagellar beating in human sperm. In *Proceedings of the 36th Annual International Conference of the IEEE Engineering in Medicine and Biology Society (EMBC)*; 26–30 August 2014; Chicago, IL, USA. IEEE: Chicago, IL, USA, 2014, pp190–193.
25 Corkidi G, Taboada B, Wood CD, Guerrero A, Darszon A. Tracking sperm in three-dimensions. *Biochem Biophys Res Commun* 2008; **373**: 125–129.
26 Frauel Y, Naughton TJ, Matoba O, Tajahuerce E, Javidi B. Three-dimensional imaging and processing using computational holographic imaging. *Proc IEEE* 2006; **94**: 636–653.
27 Rosen J, Brooker G. Non-scanning motionless fluorescence three-dimensional holographic microscopy. *Nat Photon* 2008; **2**: 190–195.
28 Rivenson Y, Stern A, Javidi B. Overview of compressive sensing techniques applied in holography [Invited]. *Appl Opt* 2013; **52**: A423–A432.
29 Gorocs Z, Ozcan A. On-chip biomedical imaging. *IEEE Rev Biomed Eng* 2013; **6**: 29–46.
30 Shan MG, Kandel ME, Popescu G. Refractive index variance of cells and tissues measured by quantitative phase imaging. *Opt Express* 2017; **25**: 1573–1581.
31 Kandel ME, Teng KW, Selvin PR, Popescu G. Label-free imaging of single microtubule dynamics using spatial light interference microscopy. *ACS Nano* 2017; **11**: 647–655.

32 Indebetouw G, Tada Y, Rosen J, Brooker G. Scanning holographic microscopy with resolution exceeding the Rayleigh limit of the objective by superposition of off-axis holograms. *Appl Opt* 2007; **46**: 993–1000.
33 Moon I, Javidi B. Three-dimensional identification of stem cells by computational holographic imaging. *J Roy Soc Interface* 2007; **4**: 305–313.
34 Xu WB, Jericho MH, Meinertzhagen IA, Kreuzer HJ. Digital in-line holography for biological applications. *Proc Natl Acad Sci USA* 2001; **98**: 11301–11305.
35 Matrecano M, Paturzo M, Ferraro P. Extended focus imaging in digital holographic microscopy: a review. *Opt Eng* 2014; **53**: 112317.
36 Colomb T, Pavillon N, Kühn J, Cuche E, Depeursinge C *et al.* Extended depth-of-focus by digital holographic microscopy. *Opt Lett* 2010; **35**: 1840–1842.
37 Di Caprio G, Gioffrè MA, Saffioti N, Grilli S, Ferraro P *et al.* Quantitative label-free animal sperm imaging by means of digital holographic microscopy. *IEEE J Sel Top Quantum Electron* 2010; **16**: 833–840.
38 Memmolo P, Di Caprio G, Distante C, Paturzo M, Puglisi R *et al.* Identification of bovine sperm head for morphometry analysis in quantitative phase-contrast holographic microscopy. *Opt Express* 2011; **19**: 23215–23226.
39 Merola F, Miccio L, Memmolo P, Di Caprio G, Galli A *et al.* Digital holography as a method for 3D imaging and estimating the biovolume of motile cells. *Lab Chip* 2013; **13**: 4512–4516.
40 Di Caprio G, El Mallahi A, Ferraro P, Dale R, Coppola G *et al.* 4D tracking of clinical seminal samples for quantitative characterization of motility parameters. *Biomed Opt Express* 2014; **5**: 690–700.
41 Jikeli JF, Alvarez L, Friedrich BM, Wilson LG, Pascal R *et al.* Sperm navigation along helical paths in 3D chemoattractant landscapes. *Nat Commun* 2015; **6**: 7985.
42 Wilson LG, Carter LM, Reece SE. High-speed holographic microscopy of malaria parasites reveals ambidextrous flagellar waveforms. *Proc Natl Acad Sci USA* 2013; **110**: 18769–18774.
43 Su TW, Erlinger A, Tseng D, Ozcan A. Compact and light-weight automated semen analysis platform using lensfree on-chip microscopy. *Anal Chem* 2010; **82**: 8307–8312.
44 Su TW, Choi I, Feng JW, Huang K, McLeod E *et al.* Sperm trajectories form chiral ribbons. *Sci Rep* 2013; **3**: 1664.
45 Su TW, Choi I, Feng JW, Huang K, Ozcan A. High-throughput analysis of horse sperms' 3D swimming patterns using computational on-chip imaging. *Anim Reprod Sci* 2016; **169**: 45–55.
46 Yu X, Hong J, Liu CG, Kim MK. Review of digital holographic microscopy for three-dimensional profiling and tracking. *Opt Eng* 2014; **53**: 112306.
47 Memmolo P, Miccio L, Paturzo M, Di Caprio G, Coppola G *et al.* Recent advances in holographic 3D particle tracking. *Adv Opt Photon* 2015; **7**: 713–755.
48 Greenbaum A, Luo W, Su TW, Göröcs Z, Xue L *et al.* Imaging without lenses: achievements and remaining challenges of wide-field on-chip microscopy. *Nat Methods* 2012; **9**: 889–895.
49 Greenbaum A, Luo W, Khademhosseinieh B, Su TW, Coskun AF *et al.* Increased space-bandwidth product in pixel super-resolved lensfree on-chip microscopy. *Sci Rep* 2013; **3**: 1717.
50 Gurtner M, Zemánek J. Twin-beam real-time position estimation of micro-objects in 3D. *Meas Sci Technol* 2016; **27**: 127003.
51 Memmolo P, Finizio A, Paturzo M, Miccio L, Ferraro P. Twin-beams digital holography for 3D tracking and quantitative phase-contrast microscopy in microfluidics. *Opt Express* 2011; **19**: 25833–25842.
52 Merola F, Miccio L, Paturzo M, Finizio A, Grilli S *et al.* Driving and analysis of micro-objects by digital holographic microscope in microfluidics. *Opt Lett* 2011; **36**: 3079–3081.
53 Goodman JW. *Introduction to Fourier Optics*. New York: Roberts & Company Publishers; 2005.
54 Mudanyali O, Tseng D, Oh C, Isikman SO, Sencan I *et al.* Compact, light-weight and cost-effective microscope based on lensless incoherent holography for telemedicine applications. *Lab Chip* 2010; **10**: 1417–1428.
55 Wei QS, Luo W, Chiang S, Kappel T, Mejia C *et al.* Imaging and sizing of single DNA molecules on a mobile phone. *ACS Nano* 2014; **8**: 12725–12733.
56 Penfold LM, Holt C, Holt WV, Welch GR, Cran DG *et al.* Comparative motility of X and Y chromosome-bearing bovine sperm separated on the basis of DNA content by flow sorting. *Mol Reprod Dev* 1998; **50**: 323–327.
57 Leung C, Lu Z, Esfandiari N, Casper RF, Sun Y. Detection and tracking of low contrast human sperm tail. In: *Proceedings of the 2010 IEEE Conference on Automation Science and Engineering (CASE)*; 21–24 August 2010; Toronto, ON, USA. IEEE: Toronto, ON, USA, 2010, pp 263–268.
58 Yang HF, Descombes X, Prigent S, Malandain G, Druart X *et al.* Head tracking and flagellum tracing for sperm motility analysis. In *Proceedings of the 11th International Symposium on Biomedical Imaging (ISBI)*; 29 April–2 May 2014; Beijing, China. IEEE: Beijing, China, 2014, pp 310–313.
59 Babcock DF, Wandernoth PM, Wennemuth G. Episodic rolling and transient attachments create diversity in sperm swimming behavior. *BMC Biol* 2014; **12**: 67.
60 Afzelius B. Electron microscopy of the sperm tail results obtained with a new fixative. *J Cell Biol* 1959; **5**: 269–278.
61 Gibbons IR. Structural asymmetry in cilia and flagella. *Nature* 1961; **190**: 1128–1129.
62 Woolley DM. Interpretations of the pattern of sperm tail movements. In: Fawcett DW, Bedford JM (eds). *The Spermatozoon*. Urban & Schwarzenburg: Baltimore-Munich. 1979, pp 69–79.
63 Nosrati R, Driouchi A, Yip CM, Sinton D. Two-dimensional slither swimming of sperm within a micrometre of a surface. *Nat Commun* 2015; **6**: 8703.

This work is licensed under a Creative Commons Attribution-NonCommercial-NoDerivs 4.0 International License. The images or other third party material in this article are included in the article's Creative Commons license, unless indicated otherwise in the credit line; if the material is not included under the Creative Commons license, users will need to obtain permission from the license holder to reproduce the material. To view a copy of this license, visit http://creativecommons.org/licenses/by-nc-nd/4.0/

© The Author(s) 2018

Supplementary Information for this article can be found on the *Light: Science & Applications* website (http://www.nature.com/lsa).